AGU PUBLICATIONS

JGR

Journal of Geophysical Research: Atmospheres

RESEARCH ARTICLE
10.1002/2015JD023242

Key Points:
- Airborne eddy covariance flux measurements over oil and gas extraction regions
- Estimates of CH_4 emissions agree with the mass balance method
- Airborne eddy covariance is a powerful method to estimate oil and gas emissions

Supporting Information:
- Figures S1–S8 and Table S1

Correspondence to:
B. Yuan,
bin.yuan@noaa.gov

Citation:
Yuan, B., et al. (2015), Airborne flux measurements of methane and volatile organic compounds over the Haynesville and Marcellus shale gas production regions, *J. Geophys. Res. Atmos.*, *120*, 6271–6289, doi:10.1002/2015JD023242.

Received 10 FEB 2015
Accepted 2 JUN 2015
Accepted article online 4 JUN 2015
Published online 26 JUN 2015

Airborne flux measurements of methane and volatile organic compounds over the Haynesville and Marcellus shale gas production regions

Bin Yuan[1,2], Lisa Kaser[3], Thomas Karl[4], Martin Graus[1,2,4], Jeff Peischl[1,2], Teresa L. Campos[3], Steve Shertz[3], Eric C. Apel[3], Rebecca S. Hornbrook[3], Alan Hills[3], Jessica B. Gilman[1,2], Brian M. Lerner[1,2], Carsten Warneke[1,2], Frank M. Flocke[3], Thomas B. Ryerson[1], Alex B. Guenther[3,5], and Joost A. de Gouw[1,2,6]

[1]Chemical Sciences Division, NOAA Earth System Research Laboratory, Boulder, Colorado, USA, [2]Cooperative Institute for Research in Environmental Sciences, University of Colorado, Boulder, Colorado, USA, [3]Atmospheric Chemistry Division, National Center for Atmospheric Research, Boulder, Colorado, USA, [4]Institute of Meteorology and Geophysics, University of Innsbruck, Innsbruck, Austria, [5]Atmospheric Sciences and Global Change Division, Pacific Northwest National Laboratory, Richland, Washington, USA, [6]Department of Chemistry and Biochemistry, University of Colorado, Boulder, Colorado, USA

Abstract Emissions of methane (CH_4) and volatile organic compounds (VOCs) from oil and gas production may have large impacts on air quality and climate change. Methane and VOCs were measured over the Haynesville and Marcellus shale gas plays on board the National Center for Atmospheric Research C-130 and NOAA WP-3D research aircraft in June–July of 2013. We used an eddy covariance technique to measure in situ fluxes of CH_4 and benzene from both C-130 flights with high-resolution data (10 Hz) and WP-3D flights with low-resolution data (1 Hz). Correlation ($R = 0.65$) between CH_4 and benzene fluxes was observed when flying over shale gas operations, and the enhancement ratio of fluxes was consistent with the corresponding concentration observations. Fluxes calculated by the eddy covariance method show agreement with a mass balance approach within their combined uncertainties. In general, CH_4 fluxes in the shale gas regions follow a lognormal distribution, with some deviations for relatively large fluxes ($>10\ \mu g\ m^{-2}\ s^{-1}$). Statistical analysis of the fluxes shows that a small number of facilities (i.e., ~10%) are responsible for up to ~40% of the total CH_4 emissions in the two regions. We show that the airborne eddy covariance method can also be applied in some circumstances when meteorological conditions do not favor application of the mass balance method. We suggest that the airborne eddy covariance method is a reliable alternative and complementary analysis method to estimate emissions from oil and gas extraction.

1. Introduction

The advancement of horizontal drilling and hydraulic fracturing has promoted production of oil and natural gas in the United States (U.S.) significantly in recent years. Crude oil and natural gas production in the U.S. increased by 47.9% and 28.6%, respectively, from 2005 to 2013, making the U.S. the largest producer of oil and natural gas in the word [*Energy Information Administration*, 2013]. The processes associated with oil and natural gas extraction can lead to significant emissions of methane (CH_4), volatile organic compounds (VOCs), and nitrogen oxides ($NO_x = NO + NO_2$) into the atmosphere. Based on the inventory of greenhouse gas (GHG) emissions by the U.S. Environmental Protection Agency (EPA), production and transportation of oil and natural gas contribute 28%, 21%, and 5% of the total emissions of CH_4, nonmethane volatile organic compounds, and NO_x in the U.S., respectively [*U.S. Environmental Protection Agency*, 2014]. These emissions have large impacts on both regional air quality [*Edwards et al.*, 2014; *Kemball-Cook et al.*, 2010; *Schnell et al.*, 2009] and global climate change [*Montzka et al.*, 2011]. Emissions of some air toxics (e.g., aromatic hydrocarbons) may also affect human health for people working at or living nearby the production sites [*McKenzie et al.*, 2014].

Many studies report that emission estimates of methane and other air pollutants from oil and natural gas production are not accurately represented in current emission inventories [*Brandt et al.*, 2014; *Karion et al.*, 2013; *Miller et al.*, 2013; *Pétron et al.*, 2014]. Recent studies demonstrate that aircraft measurements are a powerful technique for estimating methane and other hydrocarbon emissions from oil and natural gas production [*Caulton et al.*, 2014; *Karion et al.*, 2013; *Peischl et al.*, 2015; *Pétron et al.*, 2014]. Aircraft measurements of targeted species in both upwind and downwind directions can be used to estimate the

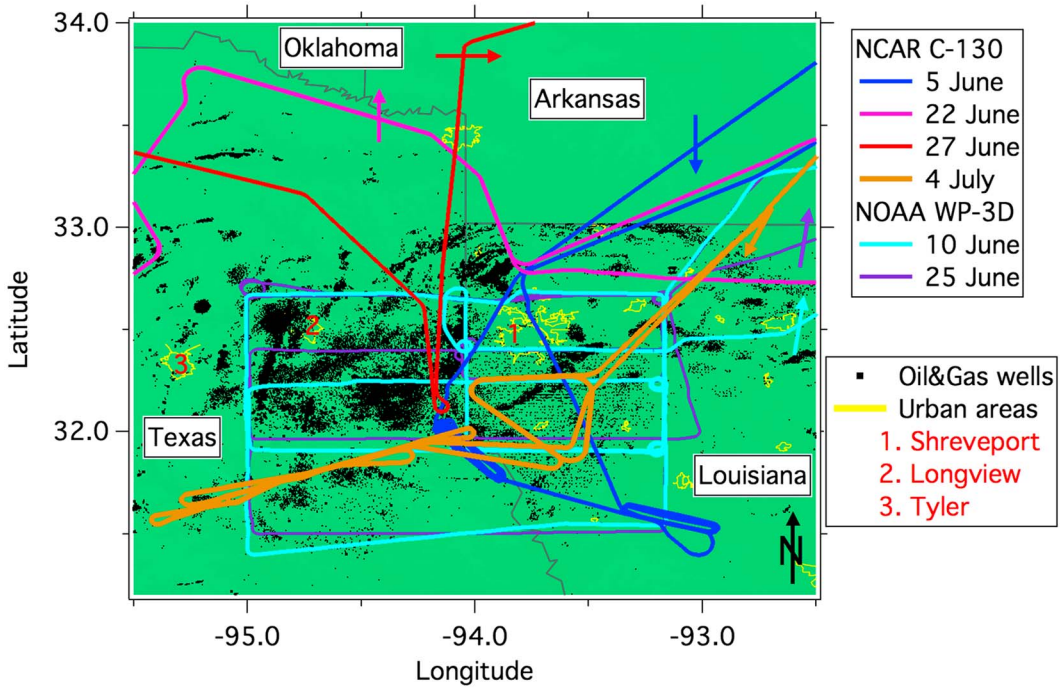

Figure 1. Flight tracks of the NCAR C-130 during NOMADSS and the NOAA WP-3D during SENEX over the Haynesville shale gas play. The black dots are the locations of oil and gas wells. The arrows on flight tracks indicate the main horizontal wind directions when the aircrafts flew in the boundary layer. The background of the graph indicates the elevation heights above sea level (same as other graphs, e.g., Figures 4 and 6), indicating a flat terrain in this region.

total emissions of the species using the mass balance method [*White et al.*, 1976]. Besides total emissions, emission patterns and emission strengths from different operation procedures, well types, and regions are possible but more difficult to obtain from aircraft observations [*Caulton et al.*, 2014]. Ground investigations of individual wells using a downwind tracer ratio method [*Allen et al.*, 2013] can help to address this issue, but this kind of research is both labor intensive and time consuming, resulting in large budgetary demands [*Brandt et al.*, 2014].

Airborne flux measurements using the eddy covariance technique provide an approach that is independent of the mass balance method. The airborne eddy covariance technique has been applied to measure fluxes of CO_2, ozone (O_3) [*Mauder et al.*, 2007; *Zulueta et al.*, 2013], and isoprene [*Karl et al.*, 2013; *Misztal et al.*, 2014] over vegetation, aromatics from urban emissions [*Karl et al.*, 2009], dust from the Sahara desert [*Rosenberg et al.*, 2014], and CH_4 from agricultural emissions [*Hiller et al.*, 2014]. The utilization of the continuous wavelet transformation (CWT) approach to calculate airborne fluxes improves the spatial resolution of flux results significantly and makes comparisons between measurements and emission inventories possible on spatial scales of several kilometers [*Karl et al.*, 2009; *Metzger et al.*, 2013; *Misztal et al.*, 2014].

In this study, airborne eddy covariance flux measurements were conducted for the first time over two shale gas production regions. We use the data sets to demonstrate the feasibility of the technique and present the results from airborne flux measurements over oil and natural gas production regions. Insights into the distributions of emission strengths from results of the eddy covariance flux measurements will also be presented.

2. Measurements and Methods

2.1. Measurements

Two aircraft campaigns (Nitrogen, Oxidants, Mercury, and Aerosol Distributions, Sources, and Sinks (NOMADSS) and Studying the Interactions Between Natural and Anthropogenic Emissions at the Nexus of Climate Change and Air Quality (Southeast Nexus (SENEX))) were conducted using the National Center for Atmospheric Research (NCAR) C-130 and NOAA WP-3D aircraft, respectively, in June and July of 2013. The two campaigns were conducted under the broader research umbrella of the Southeast Atmosphere Study. While both missions had multiple scientific objectives, both the NCAR C-130 and NOAA WP-3D flew over shale gas production regions.

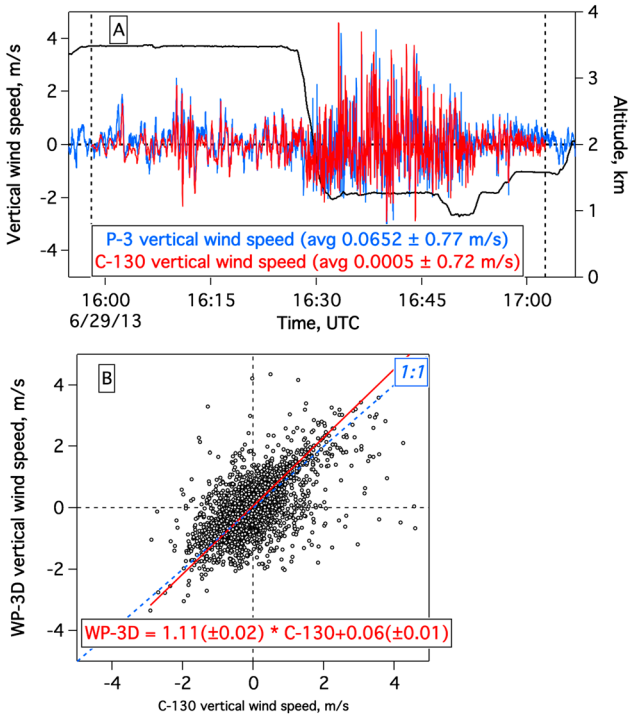

Figure 2. Comparison of vertical wind speed measurements from C-130 and WP-3D during the coordinated aircraft intercomparison flight on 29 June 2013 ((a) time series and (b) scatterplot). The black line in Figure 2a shows the flight altitudes of the two aircraft. The vertical dashed lines in the time series plot (Figure 2a) show the comparison period. The red line in the scatterplot (Figure 2b) is the linear, equally weighted, bivariate orthogonal distance regression fit to the data points (same for other linear fits in this study). The dashed blue line is the 1:1 reference line.

The Haynesville shale gas region was investigated in most detail by the two campaigns. Figure 1 shows flight tracks of the NCAR C-130 and NOAA WP-3D over the Haynesville shale gas region. The NOAA WP-3D conducted two flights (10 and 25 June) with rectangular flight tracks, aiming to derive total emissions of CH_4 in this region using the mass balance approach [*Peischl et al.*, 2015]. The C-130 flew in this area on three different flights (5 June, 27 June, and 4 July). The C-130 also flew downwind of the Haynesville shale gas play on 22 June to sample outflow from the region.

In addition to the flights over the Haynesville shale gas play, observations from several other flights are also used in this study. On 5 July, the C-130 flew over the Atlantic Ocean to sample clear marine air. On 6 July, the NOAA WP-3D flew to the Marcellus shale gas play in northeastern Pennsylvania, and a similar rectangular flight pattern was conducted to estimate CH_4 emissions (Figure S1 in the supporting information). This region accounts for over 70% of natural gas production in the Marcellus shale play in 2013 based on U.S. Energy Information Administration data (www.eia.gov). The WP-3D also flew to the Fayetteville shale play on 26 June and 8 July, and the data set on 8 July was used to calculate total CH_4 emissions in this region using the mass balance method [*Peischl et al.*, 2015], but the data will not be used in this study due to the mountainous terrain surrounding the Fayetteville shale play. Eddy covariance flux measurements over mountainous regions need additional corrections to vertical wind velocity to remove vertical motion that results from sloping topography and flow distortion [*Reba et al.*, 2009].

Payload and instrument layout of C-130 and WP-3D can be found on the NOMADSS website (https://www.eol.ucar.edu/content/c-130-layout) and SENEX website (http://www.esrl.noaa.gov/csd/projects/senex/p3payload.html), respectively. Methane (CH_4) and carbon dioxide (CO_2) were measured by wavelength-scanned cavity ring down spectroscopy on both the C-130 (Picarro G2311-f) and WP-3D (Picarro G1301-m) [*Peischl et al.*, 2012]. On the C-130, volatile organic compounds (VOCs) were measured by a proton transfer reaction–mass spectrometer (PTR-MS) [*Karl et al.*, 2013] and a Trace Organic Gas Analyzer (one 30 s sample every 2 min) [*Apel et al.*, 2010]. On the NOAA WP-3D, a PTR-MS measured a subset of VOCs online [*Warneke et al.*, 2013], and canister samples (72 canisters per flight) were also collected and analyzed after flights by a gas chromatography–mass spectrometry on ground (improved Whole Air Sampler With immediate Analysis System). During flights over oil and gas regions, the PTR-MS systems on board both the C-130 and WP-3D usually recorded 18–20 masses, each with a dwell time of 1 s, which are related to aromatics, alcohols, aldehydes, ketones, and organic acids. During the C-130 flights on 27 June and 4 July, the PTR-MS was run in flux mode, with measurements of masses attributed to benzene (*m/z* 79), toluene (*m/z* 93), isoprene (*m/z* 69), and methyl vinyl ketone + methacrolein (MVK + MACR) (*m/z* 71), each with a dwelling time of 0.1 s (Table S1 in the supporting information). Contributions of other nonbiogenic compounds (e.g., fragments from cyclohexanes) to signals of *m/z* 69 and *m/z* 71 are possible [*Warneke et al.*, 2015; *Yuan et al.*, 2014], but they are expected to be small in the two oil and gas production regions in the daytime of summer. Only flux mode data from the PTR-MS on the C-130 are used to calculate eddy covariance fluxes of benzene in this study. For the two C-130 flights on 27 June and 4 July, high-frequency CH_4 data (10 Hz) were also

acquired. Power spectral analysis of CH_4 and CO_2 signals from Picarro G2311-f instrument indicates that the instrument response may be limited to several hertz as a result of high-frequency attenuation. Winds were recorded by five-hole pressure sensors on the radome of the aircraft (Rosemount model 1221F1VL) at 25 Hz on the C-130 and at 1 Hz on the WP-3D [*Khelif et al.*, 1999]. Good agreement of measured vertical wind speeds by C-130 and WP-3D ($N = 3876$, $R = 0.61$, and slope $= 1.11 \pm 0.02$) was obtained during the coordinated aircraft intercomparison flight on 29 June 2013 (Figure 2).

2.2. Eddy Covariance Methods

An eddy covariance flux is defined as the averaged product of fluctuating terms of vertical wind speed and the concentration of a scalar. Two methods in the literature are generally used to calculate airborne eddy covariance fluxes: fast Fourier transformation (FFT) and continuous wavelet transformation (CWT). FFT can compute an average flux over a certain period or a certain flight leg for the case of aircraft measurements. CWT computes correlations with point-by-point flux outputs over a chosen bandwidth without the requirement of homogeneity or stationarity [*Misztal et al.*, 2014], which are defined as the conditions under which the statistical properties of airflow do not change with space and time [*Reba et al.*, 2009], respectively. In this study, we mainly use CWT; the FFT method is applied for the purpose of intercomparison and as a supplementary approach.

The wavelet transformation routine proposed by *Torrence and Compo* [1998] is used below. A continuous wavelet transform of a discrete sequence $x(n)$ of N data points is defined as convolution of $x(n)$ with a wavelet function [*Mauder et al.*, 2007; *Misztal et al.*, 2014]:

$$W_x(a,b) = \sum_{n=0}^{N} x(n)\psi^*_{p,a,b}(n) \tag{1}$$

where a, b, and p are the scale parameter, space parameter, and normalized factor, respectively. Parameter $\psi^*_{p,a,b}$ is the complex conjugate of the wavelet function, which is given by

$$\psi_{p,a,b} = \frac{1}{a^p}\psi\left(\frac{n-b}{a}\right) \tag{2}$$

The $\psi\left(\frac{n-b}{a}\right)$ is called the "mother wavelet," and for this study, we use the Morlet wavelet, which has been shown to be suitable for the analysis of atmospheric turbulence [*Mauder et al.*, 2007]. The settings of scales for wavelet transformation are determined according to *Torrence and Compo* [1998]. The detailed procedures of the CWT method in previous studies [*Karl et al.*, 2009, 2013] are adopted. CWT has several advantages for aircraft measurements compared to FFT method. (1) The effect of the lack of homogeneity or stationarity in aircraft measurements is minimized, as shown by measurements in an urban area [*Karl et al.*, 2009]. Measurements over oil and gas production regions would have a similar inhomogeneity issue as urban areas. (2) CWT can produce time-resolved spectral contribution to the measured flux [*Misztal et al.*, 2014]. Comparisons of CWT results with those from FFT show that flux estimates from CWT are quantitatively acceptable (usually better than 30%) [*Karl et al.*, 2009; *Mauder et al.*, 2007; *Misztal et al.*, 2014].

The segments for each calculation of CWT and FFT fluxes are selected based on minimal roll angle of the aircraft between turns and little altitude variations, following the suggestions in a recent study [*Misztal et al.*, 2014]. The periods for vertical profiles or changing altitude for another flight leg are excluded for the flux analysis. No detrending is applied in this study, and the fluctuating terms are calculated from measurements subtracted by block average for each flight segment. The lag time between the signals from the gas analyzers and vertical wind speed, introduced from either different computer clocking or sampling time from inlet to detector, was determined before the implementation of eddy covariance flux calculation [*Park et al.*, 2013]. The lag time for each flux segment is determined from the peak location of cross correlation between VOC signals and vertical wind speed by shifting VOC data points with steps according to their measurement frequency (0.1 s for C-130 and 1 s for WP-3D data). To improve the accuracy of the determined lag time, the lag time of benzene and toluene measured by PTR-MS is determined from comeasured isoprene, and the lag time of CH_4 measured by the Picarro instrument is determined from comeasured CO_2, as the fluxes of isoprene and CO_2 due to emission and uptake by vegetation were much larger in this study.

The footprint of eddy covariance fluxes defines the source contribution area of the flux measurements. The footprint of each flux point depends on wind speed, flight altitude, boundary layer height, and convective velocity [*Weil and Horst*, 1992], and it can be parameterized as

$$dx_{0.5} = 0.9\frac{uz^{2/3}z_i^{1/3}}{w^*} \tag{3}$$

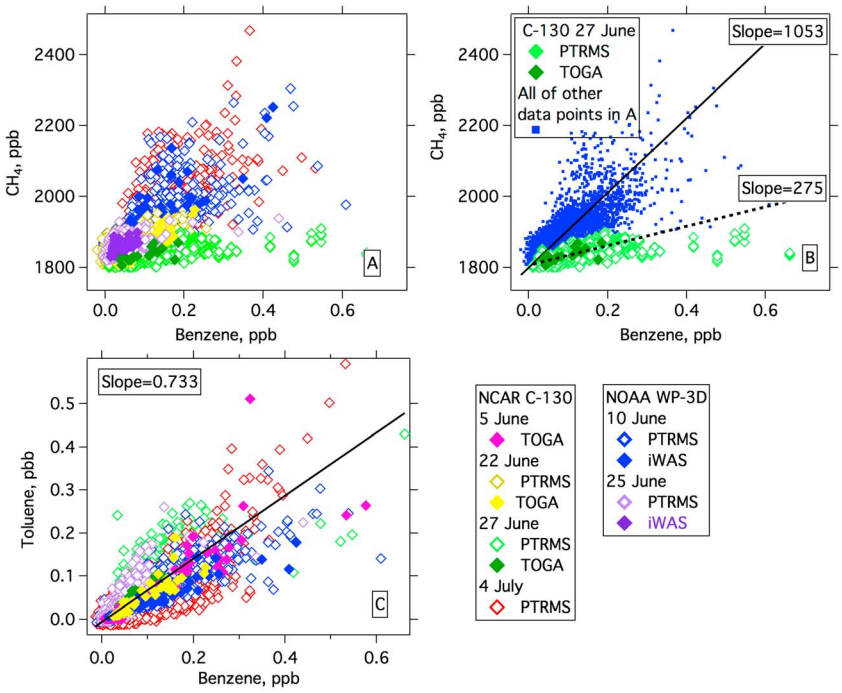

Figure 3. Scatterplots of (a and b) CH_4 versus benzene and (c) toluene versus benzene from all flights of C-130 and WP-3D over or downwind of the Haynesville shale play. The black solid lines are the linear fits to data points excluding those from the C-130 flight on 27 June. The dashed line in Figure 3b is a linear fit to data points from the C-130 flight on 27 June.

where $dx_{0.5}$ is the half width of the horizontal footprint, u is the horizontal wind speed, z is the flight altitude, z_i is the boundary layer height, and w^* is the convective velocity scale which can be determined from the sensible heat flux ($w'T'$). The half width is defined as the horizontal distance where the flux footprint falls to half of its maximum value [*Karl et al.*, 2013]. For example, a typical half width of the horizontal footprint was 2.4 km for the triangle flight legs of the C-130 flight on 4 July over the Haynesville shale gas play ($z_i = 1.8$ km, $z = 570$ m, $u = 5.2$ m/s, and $w^* = 1.6$ m/s). Recently, *Misztal et al.* [2014] proposed that the source contribution area of a flux point from aircraft measurement can be approximated by upwind-pointed half dome with the $dx_{0.5}$ as the radius of the half dome. We derive that the source contribution area for each flux point is around 9 km^2 for the triangle flight legs of the C-130 flight on 27 June. We note that some newer methods are available for the calculation of flux footprint [e.g., *Kljun et al.*, 2004]. Rough comparison between the method in *Kljun et al.* [2004] and equation (3) shows some differences up to a factor of ~2 for $z/z_i > 0.5$. However, these newer methods are more complicated than that in *Weil and Horst* [1992] and more difficult to use. Thus, we will use equation (3) for the estimation of flux footprint in this study.

3. Results and Discussions

3.1. Correlations and Enhancement Ratios of Different Species

Enhancement ratios of different VOC species can be used to identify their emission sources. Figures 3a and 3b show scatterplots of excess CH_4 mixing ratio (measured mixing ratios minus background) versus benzene from all of the C-130 and NOAA WP-3D flights over and downwind from the Haynesville shale gas region. The data points in Figure 3b are grouped into two parts based on their respective slopes: the C-130 flight on 27 June and all of other flights over the Haynesville. Methane and benzene mixing ratios were correlated for both groups ($R = 0.65$ and $R = 0.64$), albeit with some scatter. The enhancement ratio of CH_4 to benzene in all flights, except the C-130 flight on 27 June, is determined to be 1053 ± 15 ppb/ppb. This enhancement ratio is consistent with the ratios from natural gas extraction obtained in other regions (200–1700 ppb/ppb) and much larger than those reported in urban areas (Table 1). Emissions from landfills also have high enhancement ratios of CH_4/benzene ($>10^6$ ppb/ppb) [*Kim et al.*, 2006], but landfill emissions are determined to be minor methane sources in the Haynesville shale gas play [*Peischl et al.*, 2015].

Table 1. Comparison of Enhancement Ratios of CH_4 and Toluene to Benzene From Different Shale Plays and Urban Emissions

Places	CH_4/Benzene, ppb/ppb	Toluene/Benzene, ppb/ppb
Haynesville	1053 ± 15	0.733 ± 0.007
Marcellus	512 ± 20	0.829 ± 0.095
Uintah Basin	1720[a], 1485[b]	1.55[b]
Denver-Julesburg	735[c]	0.89[d]
Upper Green River Basin	233–328[e]	1.5–2.0[e]
Urban emissions	9.8[f]	2.55[g], 4.25[h]

[a] *Helmig et al.* [2014].
[b] *Warneke et al.* [2014].
[c] *Pétron et al.* [2014].
[d] *Gilman et al.* [2013].
[e] *Field et al.* [2015].
[f] Gasoline vehicle exhausts [*Kirchstetter et al.*, 1996].
[g] Urban emissions in Los Angeles [*Borbon et al.*, 2013].
[h] Urban emissions in Boston/New York City [*Warneke et al.*, 2007].

Data points on 27 June demonstrate a lower slope (275 ± 5 ppb/ppb) than those in other flights. During the flight on 27 June, winds were from the west, and the sampled air masses may have been affected by two nearby cities (Longview, TX and Tyler, TX) (Figure 1). However, methane concentrations measured during this flight should still be mainly dominated by oil and gas emissions, considering the very low emission ratio of CH_4 to benzene (9.8 ppb/ppb) from vehicle exhaust [*Kirchstetter et al.*, 1996].

Scatterplots of toluene versus benzene are shown in Figure 3c. The enhancement ratio of toluene to benzene is 0.733 ± 0.007 ppb/ppb, which is similar to the ranges of reported emission ratios in several oil and gas production regions (0.89–2.0 ppb/ppb) (Table 1) and significantly lower than that from urban emissions (2.55 ppb/ppb in Los Angeles) [*Borbon et al.*, 2013]. The agreement of enhancement ratios with those from oil and gas production emissions indicates that the main sources of these species are from oil and gas extraction activities. Enhancement ratios of CH_4 and toluene to benzene determined from the WP-3D flight over the Marcellus shale play on 6 July are also consistent with signatures of oil and gas emissions (Table 1).

3.2. Continuous Wavelet Transformation Flux Results

3.2.1. NCAR C-130

On 4 July, the C-130 flew over two different parts of the Haynesville shale play (flight track in Figure 1): (1) a triangle flight pattern at two different altitudes over the Louisiana part of the play and (2) a racetrack flight pattern at five different altitudes in Texas. The triangle flight pattern was conducted over areas with a larger well density centered in the middle of the play. The flight track and the CWT results from the triangle flight pattern are shown in Figure 4. The data gaps in Figure 4 are due to either aircraft turning when performing the flight pattern or gaps in CH_4 data mainly as a result of routine background checks and calibrations. The C-130 entered this region from the northeast and flew in a counterclockwise pattern. During the first cycle, the C-130 flew at an altitude of 570 m above ground level (agl), and a maximum CH_4 flux was detected at the beginning of the second leg (leg #2) (32.140°N, 93.968°W). In this area, a hot spot is visible in the two-dimensional wavelet cross-spectrum between CH_4 and vertical wind speed, mainly at time scales of ~32 s and ~128 s (y axis of Figure S2 in the supporting information). A benzene flux was also observed at the beginning of leg #2. CWT fluxes of CH_4 and benzene show good correlation ($R = 0.65$) with a slope of 106 ± 9 g/g (or 514 ± 44 ppb/ppb) (Figure 4c). This emission ratio is somewhat smaller than the derived enhancement ratios in Figure 3 (860 ± 10 ppb/ppb), but still lies in the ranges of shale gas regions (Table 1), indicating that fluxes of CH_4 and benzene detected at the beginning of leg #2 were from shale gas activities.

After finishing the first cycle, the C-130 flew the same flight track again at 310 m agl about 25 min later. Again, fluxes of CH_4 and benzene were detected at the beginning of leg #2 (Figure 4b), but the magnitudes of the fluxes were much smaller for both CH_4 and benzene. This variability may be attributed to (1) flux footprint was somewhat different at the two flight altitudes. The footprint widths ($dx_{0.5}$) were calculated to be 2.4 km and 1.8 km for the 570 m and 310 m flight legs, respectively. Wind directions

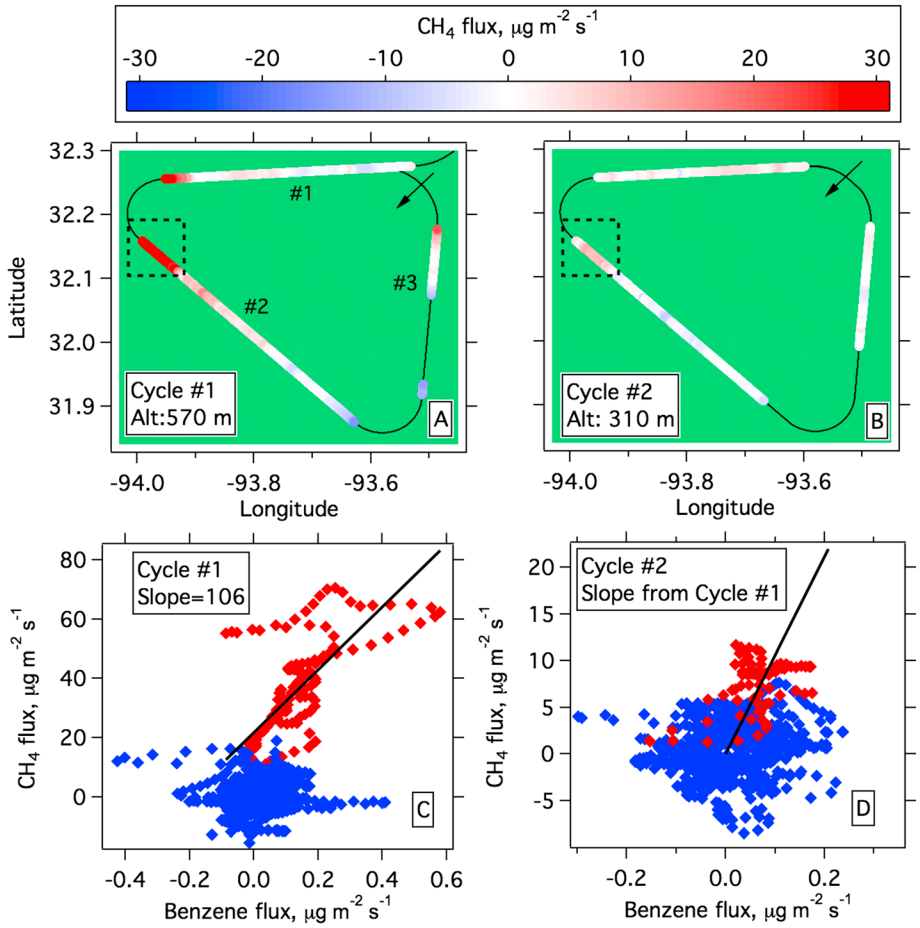

Figure 4. CWT CH_4 fluxes from the C-130 triangle flight patterns ((a) first cycle and (b) second cycle) on 4 July. The black lines indicate the C-130 flight tracks. The black arrows indicate the measured wind direction aloft in this region on 4 July. The numbers (#1, #2, and #3) in Figure 4a indicate the leg number of the triangle fight pattern. (c and d) Scatterplots of CH_4 flux versus benzene flux calculated from the triangle flight patterns. The red dots show the sampled data points, while the aircraft was in the dashed boxes in Figures 4a and 4b, respectively. The black lines in both Figures 4c and 4d are the linear fit from red dots in Figure 4c.

(35° for 510 m leg and 54° for 310 m leg) were also slightly different when the aircraft flew over this hot spot. The difference in footprints may result in larger contribution from a point source to one flight leg than another leg, as implied in the distributions of flux footprint along the upwind distance [*Kljun et al.*, 2004; *Weil and Horst*, 1992]. (2) Random errors can contribute significantly to the calculated instantaneous fluxes (see discussion in section 3.3). (3) There might be some potential variability of the emission sources, such as short-term large emissions as a result of scheduled/unscheduled venting and unloading events of shale gas facilities [*Allen et al.*, 2013]. This variability demonstrates the need for repeated measurements to obtain meaningful flux results for this small hot spot. The lower fluxes of both CH_4 and benzene from the second cycle of triangle pattern make it difficult to obtain an enhancement ratio as was obtained from the first triangle cycle.

We also observed concurrent enhancements of CWT fluxes of benzene and CH_4 during the C-130 flight on 27 June (Figure S3 in the supporting information). The flux of benzene at this hot spot (32.386°N, 94.203°W) reached a maximum of 1.1 $\mu g\, m^{-2}\, s^{-1}$. The slope of CH_4 flux versus benzene flux was 6.2 g/g (or 30 ppb/ppb), which is significantly lower than the signature from oil and gas extraction and approaches that from urban emissions. However, we note that the two nearest cities (Tyler and Longview, TX) are both too far away (~50 and ~100 km) to account for this flux hot spot, since half widths of the horizontal footprint of the flux measurements from aircraft are in the range of several kilometers (2.4 km for this flight) [*Karl et al.*, 2013]. Measurements of CO, a combustion tracer, also suggest that this plume was not

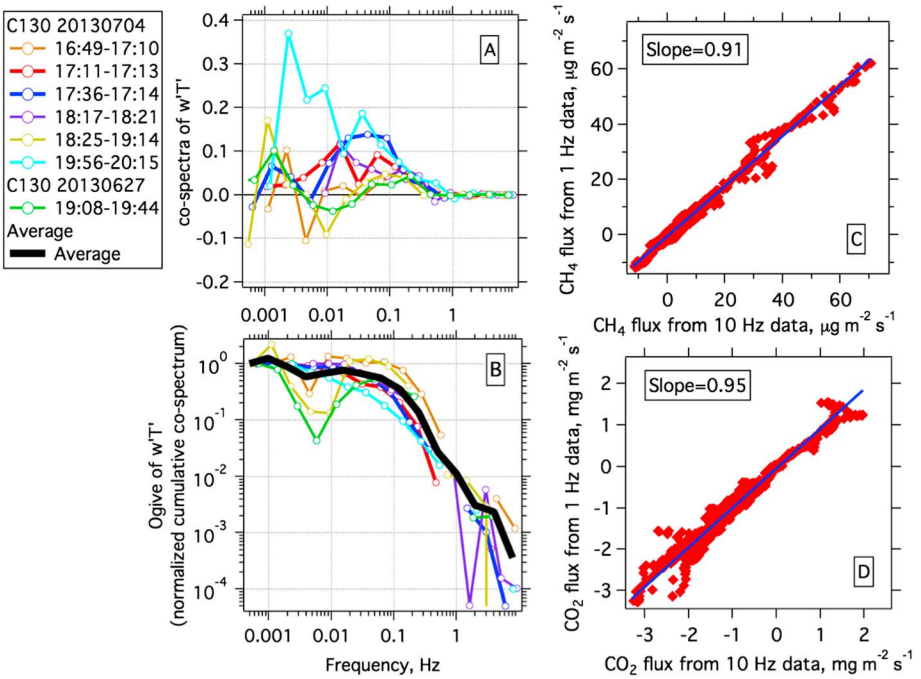

Figure 5. (a) Cross spectra and (b) ogives (normalized cumulative cross spectra) of *w'T'* from the C-130 flights on 27 June and 4 July. The black curve in Figure 5b indicates the average from all of the individual ogives. (c and d) Scatterplots of CH_4 and CO_2 fluxes calculated using 10 Hz data versus those calculated using 1 Hz data during the first triangle pattern of the C-130 flight on 4 July. The blue lines show the linear fits to the data points.

from urban emissions. These elevated benzene and CH_4 fluxes may come from some other activities or point source in this area.

3.2.2. NOAA WP-3D

Both CH_4 concentration and vertical wind speed were recorded at 1 Hz on the NOAA WP-3D. To investigate the feasibility of using 1 Hz data for turbulent flux calculations, spectral analysis is performed to determine the length and time scales of eddies that contribute to the eddy covariance flux. Figure 5 shows FFT cross spectra of vertical wind speed and potential temperature (*w'T'*) from C-130 measurements on 27 June and 4 July. As shown in Figure 5a, cross spectra of *w'T'* over different flight legs during the two flights are quite variable. Normalized cumulative cross spectra, commonly referred to as ogives, are calculated and plotted in Figure 5b. An averaged ogive is determined from individual curves to reduce variability. The flux of *w'T'* is mainly contributed by eddies with frequencies in the range of 0.01 Hz–1 Hz. The energy flux of *w'T'* carried by eddies with frequency greater than 1 Hz is only around 1% of the total flux. Eddy covariance fluxes of CH_4 and CO_2 calculated using 1 Hz aircraft data are 9% and 5%, respectively, lower than those determined from 10 Hz data during the first triangle pattern of the C-130 flight on 4 July, as shown in Figures 5c and 5d. Although the two different calculations obtain slightly different numbers (1% versus 5–9%), both calculations indicate that using 1 Hz data measured by aircraft at several hundred meter altitude to calculate eddy covariance flux should impose only small systematic errors ($<$10%). This result is consistent with the conclusions from aircraft measurements over the Sahara desert in the work of *Rosenberg et al.* [2014] and above California oak forests in the work of *Karl et al.* [2013]. From Figure 5b, we also conclude that a time scale of 1000 s will be enough to capture the largest eddies in the Haynesville shale gas play. This time scale corresponds to a flight leg of 100 km, at typical aircraft speeds of 100 m/s in the boundary layer for both the C-130 and the WP-3D.

The above analysis indicates that the CH_4 measurement data collected at 1 Hz on board the NOAA WP-3D can be used to calculate fluxes in the shale gas regions. Figure 6 shows CWT fluxes of CH_4 calculated from WP-3D flights on 10 and 25 June. From the plots, the locations of many hot spots of CH_4 fluxes are visible. For many of these flux hot spots, large facilities (e.g., gas processing plants and compressor stations) are identified close to the sampling locations (usually 0–3 km), based on visual inspections of Google Earth images. For example,

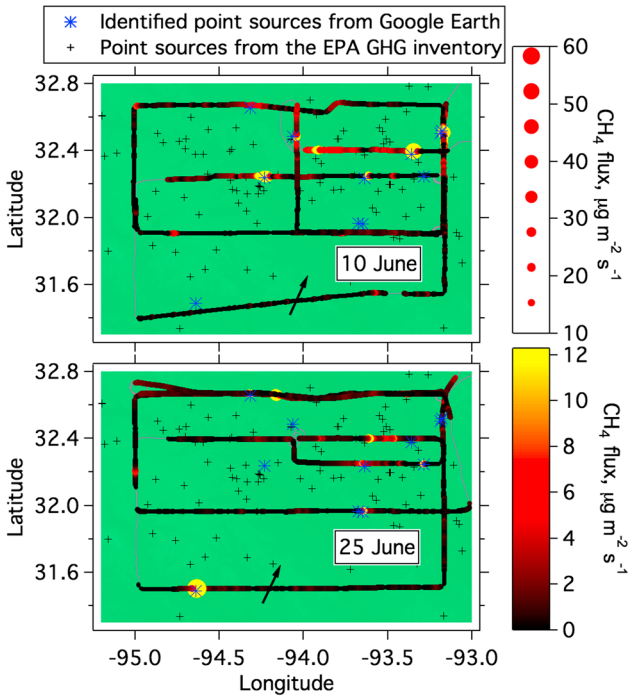

Figure 6. CWT fluxes of CH_4 for the WP-3D flight on 10 and 25 June 2013. The gray lines indicate the flight tracks of the WP-3D. The blue markers indicate the locations of large facilities identified from Google Earth images. Point sources from the 2012 EPA GHG inventory are shown in black crosses. Note that the locations of the point sources have been modified by visual inspection of Google Earth images [*Peischl et al.*, 2015]. The black arrows show the horizontal wind directions during the flights.

a large facility (31.488°N, 94.638°W) was identified 1.6 km upwind of a CH_4 flux hot spot (31.502°N, 94.635°W), observed at ~17:30 P.M. UTC (~12:30 P.M. local time) on 25 June (Figure S4 in the supporting information). Figure 7 shows a time series of CWT CH_4 fluxes on 25 June. Hot spots in Figure 6 correspond to peak flux values in the time series plot (larger than $5\,\mu g\,m^{-2}\,s^{-1}$) (see Figure 7). Besides these spikes, the CWT analysis suggests general upward fluxes of CH_4 (even though at lower magnitudes) from the region. Some periods associated with negative CH_4 fluxes are also obtained (as low as $-2.5\,\mu g\,m^{-2}\,s^{-1}$), which is due to geophysical variability of the instantaneous flux measurements. To understand the range of CH_4 fluxes, statistical analyses of CWT instantaneous fluxes are described in the next section.

3.3. Statistical Analysis of CWT Instantaneous Fluxes

3.3.1. Cases With Zero Average Flux

To investigate the distribution of random errors in calculation of CWT instantaneous fluxes and therefore the quality of the derived emission flux, we take two cases where no significant CH_4 flux is expected or observed: one is measurements in the boundary layer over the ocean, where methane is at its background and vertical fluxes are very small, and the other is a synthetic data set associated with Gaussian random errors for both concentration and vertical wind speed, resulting in a net eddy covariance flux of zero.

On 5 July, the NCAR C-130 flew over the Atlantic Ocean, and measurements were made at different altitudes in the marine boundary layer (Figure S5 in the supporting information). Measured CH_4 concentrations were 1822 ± 1 ppb, indicating a pristine environment without significant enhancement above the regional background of the western Atlantic Ocean (http://esrl.noaa.gov/gmd/dv/iadv/graph.php?code=BMW). The same method used to calculate CWT flux as for the other shale gas play flights is used for the marine CH_4 data. Even though the expected CH_4 flux over open ocean is very small ($3.2–6.3 \times 10^{-5}\,\mu g\,m^{-2}\,s^{-1}$) [*Rhee et al.*, 2009], both positive and negative CH_4 fluxes were determined (Figure S5). These positive and negative CH_4 fluxes are attributed to random errors in the CWT calculation and the measurement errors of the methane mixing ratios and the vertical wind speed. Figure 8a shows a histogram of the derived CH_4 fluxes. The distribution is centered on zero, reflecting the absence of a detectable methane flux by this method. Fitting using different functions to the histogram indicates that the Voigt function best describes the distribution of the CH_4 flux. We also tried a Gaussian function to fit the data points, but it did

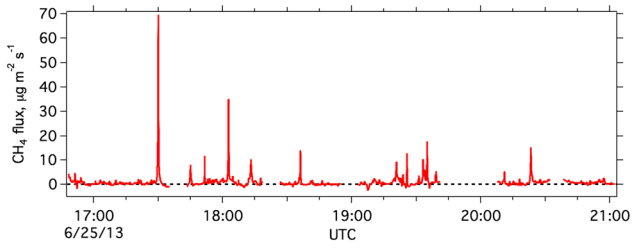

Figure 7. Time series of CWT instantaneous fluxes of CH_4 from the WP-3D flight on 25 June 2013. The dashed line indicates zero flux.

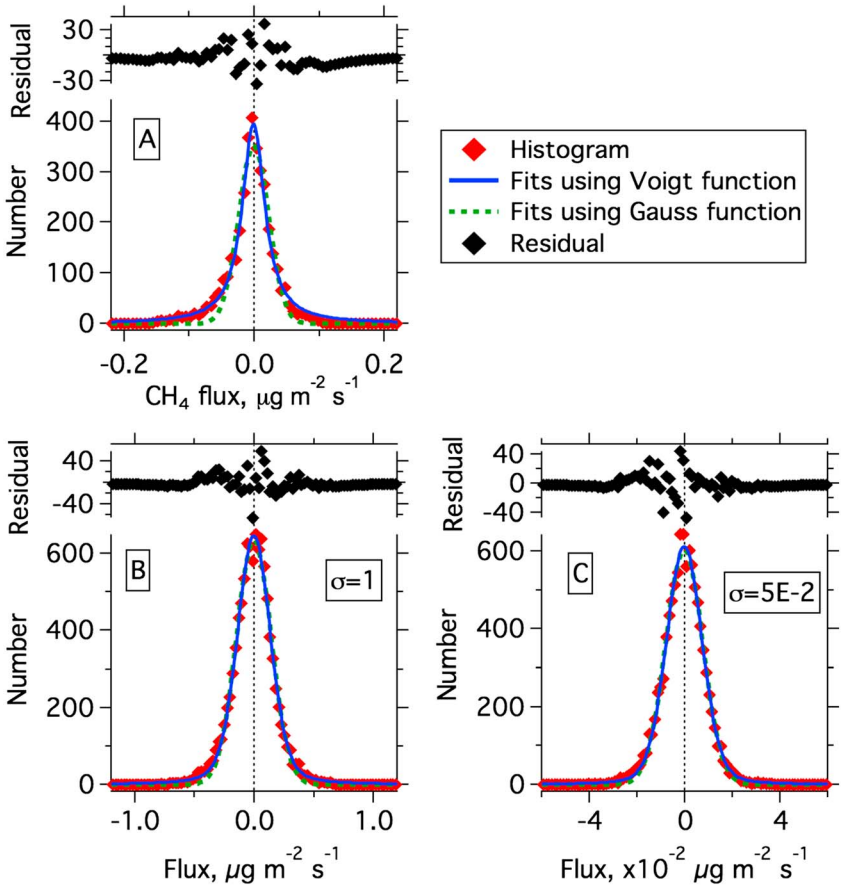

Figure 8. (a) Histogram of CH_4 flux from a C-130 flight on 5 July 2013 over a pristine section of the Atlantic Ocean, where very low CH_4 flux is expected. (b and c) Histograms of CWT flux results from the synthetic data sets. The dashed green lines indicate the Gaussian fits to data points, whereas the blue solid lines indicate the Voigt fits to data points. The black points are the residuals from Voigt fits. The numbers in the graphs are the standard deviations of input concentrations (see text).

not describe the long tails of the distributions (e.g., Figure 8). The fitted Voigt curve shows a peak location (x_0) at $1.1 \pm 0.3 \times 10^{-3}$ μg m^{-2} s^{-1} and a half width at half maximum (HWHM) of 2.2×10^{-2} μg m^{-2} s^{-1}. The ratio between x_0 and HWHM (x_0/HWHM) is 5%, suggesting that this fitted Voigt curve follows a near-zero-centered distribution.

As a second test case, we created a synthetic data set following a Gaussian distribution. First, we created a time series of vertical wind speed (0 ± 1 m/s). Second, a series of CH_4 concentrations with the same average (1850 ppb) but different standard deviations (ranging from 0.05 ppb to 4 ppb) are prescribed. Random normally distributed noise was imposed on both synthetic time series. The histograms of the calculated CWT fluxes are shown in Figures 8b and 8c (also in Figure S6 in the supporting information). Similar to Figure 8a, a Voigt function describes the histogram structures of CWT fluxes from the synthetic data sets reasonably well. The x_0/HWHM ratios for different fitted Voigt curves are between 0.4% and 4.4%. To avoid undesired correlation between vertical wind speed and concentration from single synthetic data set, an ensemble ($N = 20$) of synthetic data sets is constructed using different random seeds and similar results are obtained, as discussed above.

Based on investigations of pristine marine boundary layer data and synthetic data, we conclude that (1) in the case of a net zero flux, the distributions of instantaneous fluxes calculated by CWT is well described by a Voigt function, (2) the fitted Voigt curve represents the combined effect of geophysical variability and random noise in CWT calculations, and (3) the fitted Voigt curves center near zero for a net zero flux.

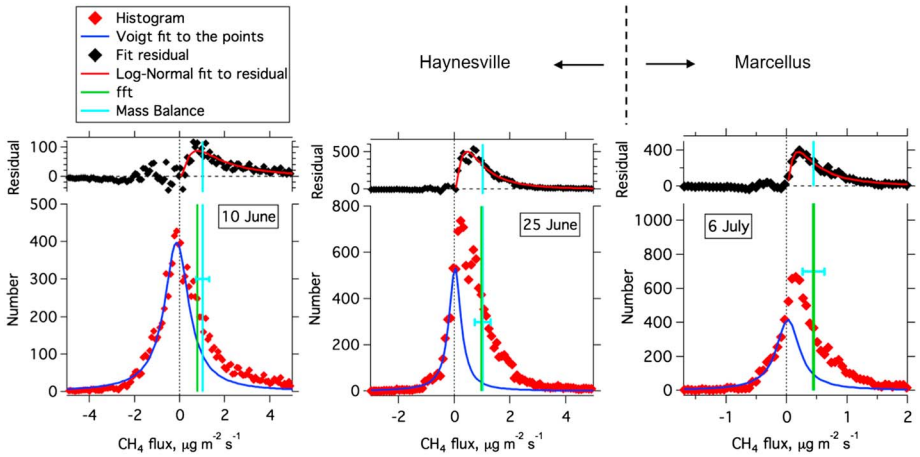

Figure 9. Histograms of CWT CH_4 fluxes from the WP-3D flights on (left) 10 June and (middle) 25 June over the Haynesville shale play and on (right) 6 July over the Marcellus shale play. The blue curves are the Voigt fits to data points with fluxes lower than or equal to zero. The black points are the residuals from Voigt fits. The green sticks are the calculated CH_4 flux using the FFT method. The light blue sticks indicate the emission estimates from the mass balance method on 25 June for the Haynesville shale play and on 6 July for the Marcellus shale play [*Peischl et al.*, 2015]. The light blue error bars indicate the uncertainties of the estimates from the mass balance method.

Random errors in CWT instantaneous fluxes may arise from several aspects: (1) concentration variability that is not due to turbulent mixing, e.g., spatial difference in the case of aircraft measurements and (2) random instrument noise for both gas concentration and wind measurements. The CWT method is a mathematical calculation procedure; thus, the combined effect of these random errors will eventually propagate in the final CWT results.

3.3.2. Cases With Nonzero Flux

Figure 9 shows histograms of CWT instantaneous fluxes of CH_4 inferred from the NOAA WP-3D measurements on 10 and 25 June over the Haynesville shale play and on 6 July over the Marcellus shale play. It is clear that the histograms in Figure 9 show a positive bias, indicative of a net upward flux. Based on the analysis in the previous section, random errors from CWT are represented by a zero-centered Voigt curve. Since a significant deposition flux of CH_4 is not expected [*Born et al.*, 1990], we apply Voigt fits to data points that correspond to CH_4 fluxes lower or equal to zero to represent random error from the CWT calculation. Residuals from the Voigt fits for CH_4 fluxes lower or equal to zero are fluctuating around zero, but positive residuals are clearly observed on the positive side of the *x* axis (especially larger than $1\,\mu g\,m^{-2}\,s^{-1}$ in both plots). Since random errors in the CWT calculation are subtracted from the fitted Voigt curves, the residuals on the positive side of the *x* axis are interpreted as average emission fluxes from shale gas wells and facilities.

Random errors in the CWT instantaneous fluxes affect not only the CH_4 flux from shale gas extraction activities but also all other CWT flux calculations. The histogram of CWT instantaneous fluxes of *m/z* 69 (isoprene + fragments from cyclohexanes) calculated from a C-130 flight over the Haynesville shale play on 4 July is shown in Figure 10. We note that *m/z* 69 should mainly come from vegetation emissions of isoprene rather than oil and gas emissions (see section 2.1). Derived negative fluxes of isoprene are smaller but are still visible. A fit using the Voigt function is also conducted to isoprene fluxes that are lower or equal to zero. A much lower fitted random error from the CWT calculation of isoprene fluxes is obtained. The main difference between the case of isoprene and that of CH_4 is that CH_4 flux measurements are more affected by inherent random errors, due to the high atmospheric CH_4 background and variability of the background caused by a long lifetime compared to isoprene.

Although the distribution of random errors in instantaneous fluxes is derived here, it is not possible to subtract random errors from each calculated data point of instantaneous flux. In spite of this, the confidence level to attribute each instantaneous flux to real emission could be derived from the fitting results in Figure 9. Evidently, an instantaneous flux of CH_4 at $2.0\,\mu g\,m^{-2}\,s^{-1}$ determined on 25 June is more statistically significant than an instantaneous flux of methane at $0.2\,\mu g\,m^{-2}\,s^{-1}$ (Figure 9b), as the

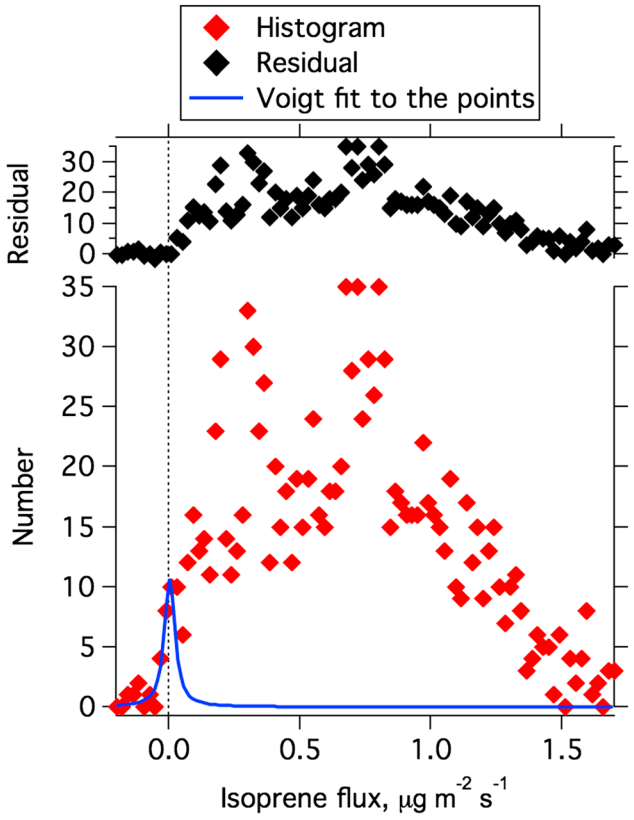

Figure 10. Histogram of CWT fluxes of isoprene measured on 4 July by the C-130 over the Haynesville shale play. The blue line is the Voigt fit to the data points lower or equal to zero. The black points are the residuals from Voigt fit.

fitted random errors (Voigt curve) account for 8% and 55% of the total measured data points at 2.0 and 0.2 $\mu g\,m^{-2}\,s^{-1}$, respectively.

In summary, the statistical analysis on the distribution of calculated instantaneous CWT fluxes is a useful technique for small fluxes or when random errors contribute significantly to the derived instantaneous fluxes. The results from the analysis are used as an indicator of positive CH_4 fluxes and a quick evaluation on the statistical significance for a given flux level to be real emissions. In addition, the statistical analysis can separate the distribution of random errors from that of emission fluxes. The implication from the distribution of the derived emission fluxes will be discussed in section 3.4.3.

3.4. Methane Emissions and Its Distribution

3.4.1. Uncertainty Analysis of Airborne Eddy Covariance Fluxes

Table 2 shows the CWT and FFT methane fluxes determined from different flights. Benzene fluxes will not be considered further, because the derived benzene fluxes are limited to only two C-130 flights. The values for CWT fluxes in Table 2 are the arithmetic means of instantaneous CWT fluxes for the respective periods over shale gas regions. The uncertainties of the averaged CWT and FFT fluxes in certain measured periods shown in Table 2 (usually <30%) are estimated from uncertainties in measured concentrations (<1%), systematic error (2–5%), and random error (around 20%) of airborne fluxes. The calculations of systematic error and random error for averaged fluxes in certain periods are shown in previous studies [*Karl et al.*, 2009, 2013; *Lenschow et al.*, 1994]. Using 1 Hz data of methane and vertical wind in WP-3D flights may contribute uncertainties of measured fluxes, and they are not accounted here.

The mass conservation equation of a scalar in the atmosphere is expressed as [*Aubinet et al.*, 2012]

$$\frac{\partial C}{\partial t} + U\frac{\partial C}{\partial x} + \frac{\partial F_{EC}}{\partial z} = S \tag{4}$$

where C is the mean concentration of the scalar, U is the mean horizontal wind speed, F_{EC} is the turbulent flux, and S is the source and sink term in the atmosphere, which is essentially zero for long-lived species (e.g., CH_4) at the time scales of convective mixing in the boundary layer. The three parts in the left-hand side of the equation are storage term (concentration change), horizontal advection, and eddy covariance flux divergence, respectively. After integrating equation (4) from ground to an altitude of z and rearranging it, the surface emission flux (F_S) can be described as

$$F_s = \int_0^z \frac{\partial C}{\partial t} + \int_0^z U\frac{\partial C}{\partial x} + F_{EC} = \int_0^z \frac{\partial C}{\partial t} + \frac{z}{z_i} \times F_{HA} + F_{EC} \tag{5}$$

where F_{EC} is the eddy covariance flux measured at an altitude of z, F_{HA} is the horizontal advection flux, and z_i is the boundary layer height. Specially, when $z = z_i$, we get

Table 2. Summary of CH_4 Fluxes From the C-130 and WP-3D Flights Over the Shale Plays

	Haynesville Flights (C-130)			Haynesville Flights (WP-3D)		Marcellus Flight (WP-3D)
Flight Dates	27 June	4 July (TRI)[a]	4 July (RT)[b]	10 June	25 June	6 July
Mass balance[c], $\mu g\,m^{-2}\,s^{-1}$	(not applicable) NA	NA	NA	NA	1.02 ± 0.29	0.44 ± 0.18
Horizontal advection flux[c], $\mu g\,m^{-2}\,s^{-1}$	NA	NA	NA	NA	0.81 ± 0.27	0.39 ± 0.15
FFT[d], $\mu g\,m^{-2}\,s^{-1}$	0.95 ± 0.22	0.53 ± 0.12	0.61 ± 0.17	0.78 ± 0.15	0.97 ± 0.21	0.44 ± 0.09
CWT[d], $\mu g\,m^{-2}\,s^{-1}$	0.98 ± 0.23	0.98 ± 0.22	0.66 ± 0.18	1.05 ± 0.20	1.00 ± 0.21	0.42 ± 0.09
CWT after correction, $\mu g\,m^{-2}\,s^{-1}$	NA	NA	NA	NA	1.23 ± 0.27	0.64 ± 0.13
HWHM of Voigt curve, $\mu g\,m^{-2}\,s^{-1}$	0.73	2.59	0.76	0.63	0.26	0.23
Voigt curve/measurements[e], %	60	94	95	77	39	51
HER fractions[f], %	NA	NA	NA	NA	26	45
THP fractions[g], %	NA	NA	NA	39	28	18

[a]Triangle patterns.
[b]Racetrack patterns.
[c]Values are derived from the total emission rates in *Peischl et al.* [2015] and the targeted areas of the two shale gas plays (see texts).
[d]The values after plus-minus sign are the uncertainties of the calculated fluxes (see text in section 3.4.1).
[e]The fraction of the area under the fitted Voigt curve to the total area under the measurements, which is an indicator for random errors in the CWT instantaneous fluxes.
[f]HER: high-emission regions (see section 3.4.3).
[g]THP: ten highest peaks (see section 3.4.3).

$$F_s = \int_0^{z_i} \frac{\partial C}{\partial t} + \int_0^{z_i} U \frac{\partial C}{\partial x} + F_{EC} = \int_0^{z_i} \frac{\partial C}{\partial t} + F_{HA} + F_{Entrainment} \tag{6}$$

where $F_{Entrainment}$ is the entrainment flux on the top of boundary layer. We note that the horizontal advection flux (and other flux terms) has a unit of $\mu g\,m^{-2}\,s^{-1}$ in this study. As mentioned earlier, *Peischl et al.* [2015] used the mass balance method to determine the total emission fluxes and horizontal advection fluxes of CH_4 from both the Haynesville and Marcellus shale plays (Table 2), based on measurements conducted by the WP-3D on 25 June and 6 July, respectively. To make the results in this study and those from the mass balance method in *Peischl et al.* [2015] comparable, we divide the results in *Peischl et al.* [2015] by the targeted areas of the two shale gas plays enclosed by the upwind and downwind transects ($2.2 \times 10^4\,km^2$ in the Haynesville and $9.4 \times 10^3\,km^2$ in the Marcellus) to transfer the unit to $\mu g\,m^{-2}\,s^{-1}$.

As shown by the equation (5), storage terms and horizontal advection flux need to be considered to connect the measured airborne eddy covariance fluxes with surface emissions (F_S). From equation (4), the underestimation of surface flux from measurements made at altitude can be derived from flux divergence by measuring eddy covariance flux at multiple altitudes [*Karl et al.*, 2013]. Flight legs at multiple altitudes to estimate flux divergence were not a focus of this study, especially for the WP-3D flights that only occurred at a single altitude. Instead, we use the horizontal advection flux from *Peischl et al.* [2015] and concentration drift to constrain the underestimation in this study (equation (5)). Here we use the WP-3D flight on 25 June as an example to discuss this issue.

1. The fraction of the underestimate of surface emissions due to horizontal advection flux (f_{HA}) could be derived from equations (5) and (6):

$$f_{HA} = \frac{z}{z_i} \times \frac{F_{HA}}{F_s} = \frac{z}{z_i} \times \frac{F_{HA}}{\int_0^{z_i} \frac{\partial C}{\partial t} + F_{HA} + F_{Entrainment}} \tag{7}$$

As horizontal advection flux is usually much larger than storage term and entrainment flux [*Gordon et al.*, 2015], f_{HA} can be approximated to be z/z_i for most of the cases. For $z/z_i = 0.35 \pm 0.07$ (25 June WP-3D flight) and $F_{HA}/F_s = 0.8$, using 0.35 as the correction fraction only introduces an error of 7% to the estimated surface emissions. Although the alternative is available, we derive the influence of horizontal advection from the estimates of total horizontal advection fluxes by the mass balance method in *Peischl et al.* [2015] (row 4 in Table 2), for the sake of more accurate estimation. Combining with the flight altitude (z) and boundary layer height (z_i), the difference between airborne eddy covariance flux and surface emission flux

is $0.28 \pm 0.06\ \mu g\ m^{-2}\ s^{-1}$. Airborne flux measurements at lower altitude will be helpful to reduce the influence of horizontal advection.

2. We observed very little change of CH_4 concentration over time during the 25 June flight (−0.5 ppb/h). This concentration change is translated to a flux of $-0.05\ \mu g\ m^{-2}\ s^{-1}$ by integrating from the ground to the measurement altitude (500 m).

In summary, the airborne CH_4 eddy covariance fluxes measured during the WP-3D flight on 25 June are likely a lower limit of surface emissions. The underestimation is calculated to be $0.23 \pm 0.06\ \mu g\ m^{-2}\ s^{-1}$, or the fluxes measured at altitude are 17–26% lower than the surface emissions. Using the same procedures as Haynesville, we determine that the airborne CH_4 fluxes derived from eddy covariance on 6 July over the Marcellus shale gas play are 43–62% ($0.22 \pm 0.04\ \mu g\ m^{-2}\ s^{-1}$) lower than the surface emissions at our best estimate. The underestimation percentage in the flight of 6 July is higher than that on 25 June, since the WP-3D flew at higher altitudes relative to the boundary layer height on 6 July ($z/z_i = 0.5 \pm 0.1$).

3.4.2. Methane Emission Strengths

The CH_4 fluxes determined from different methods, which are tabulated in Table 2, can be compared with each other. Fluxes calculated by FFT and CWT agree with each other within 30% for various flights, except for the triangle pattern during the C-130 flight on 4 July. The large difference between FFT and CWT during this period may be due to the effect of inhomogeneities on the FFT method [*Misztal et al*., 2014], as a large peak of CH_4 fluxes were detected (see section 3.2.1). Thus, CWT flux may be considered more reliable for this period.

The eddy covariance fluxes obtained in this study can be compared with the results from the mass balance method obtained by *Peischl et al.* [2015]. We note that the source contribution area of the mass balance and eddy covariance methods are different, although the same data sets are used: the mass balance method integrates the emissions in the areas enclosed by upwind and downwind flight legs, whereas the source contribution area of the eddy covariance method approximately comprises the projected upwind-pointed half domes with the radius as half widths of the horizontal footprint along the flight tracks [*Misztal et al*., 2014]. Based on footprint analysis, we roughly estimate that the total source contribution areas along the flight tracks for the eddy covariance method are in the range of $1–3 \times 10^3\ km^2$ in the Haynesville flights and $0.7–2.2 \times 10^3\ km^2$ in the Marcellus flight, both of which are small percentages (5–20%) of the targeted areas of the mass balance method in the two shale regions ($2.2 \times 10^4\ km^2$ in the Haynesville and $9.4 \times 10^3\ km^2$ in the Marcellus). The small percentages of total areas sampled by eddy covariance fluxes in both regions may result in larger uncertainties when extrapolating the eddy covariance numbers to the entire region. As we did not selectively sample specific part of the regions or any large facilities during the aircraft measurements, we presume that the eddy covariance estimates from source contribution areas equivalent to 5–20% of each basin are representative of the whole shale gas extraction basins (Haynesville and northeastern Marcellus).

As shown in previous section, the airborne eddy covariance fluxes measured at flight altitude may underestimate the surface methane emission fluxes. Surface emission fluxes inferred from eddy covariance measurements are calculated to be $1.23 \pm 0.27\ \mu g\ m^{-2}\ s^{-1}$ in the Haynesville and $0.64 \pm 0.13\ \mu g\ m^{-2}\ s^{-1}$ in the Marcellus after correction of the underestimation (Table 2). The total emission fluxes estimated from the mass balance method for 25 June flight (Haynesville) and the 6 July flight (Marcellus) are $1.02 \pm 0.29\ \mu g\ m^{-2}\ s^{-1}$ and $0.44 \pm 0.18\ \mu g\ m^{-2}\ s^{-1}$, respectively [*Peischl et al*., 2015]. Although the estimates from the eddy covariance method are somewhat higher than those from the mass balance method, the differences are both within the combined uncertainties of the eddy covariance method and the mass balance method. The reasonable agreement between the eddy covariance and mass balance methods indicates that the airborne eddy covariance method could be a reliable technique to estimate emissions from oil and gas extraction. The eddy covariance method also has several advantages that are described in the following paragraphs.

The flight patterns of the WP-3D on 10 and 25 June over the Haynesville shale play were quite similar (Figure 1). Eddy covariance CH_4 fluxes for the two flights compared well with each other for both FFT and CWT calculations, implying that there was no large day-to-day variation of CH_4 emissions with regard to the sampled areas along the flight tracks. A comparison of estimates by the mass balance method from different

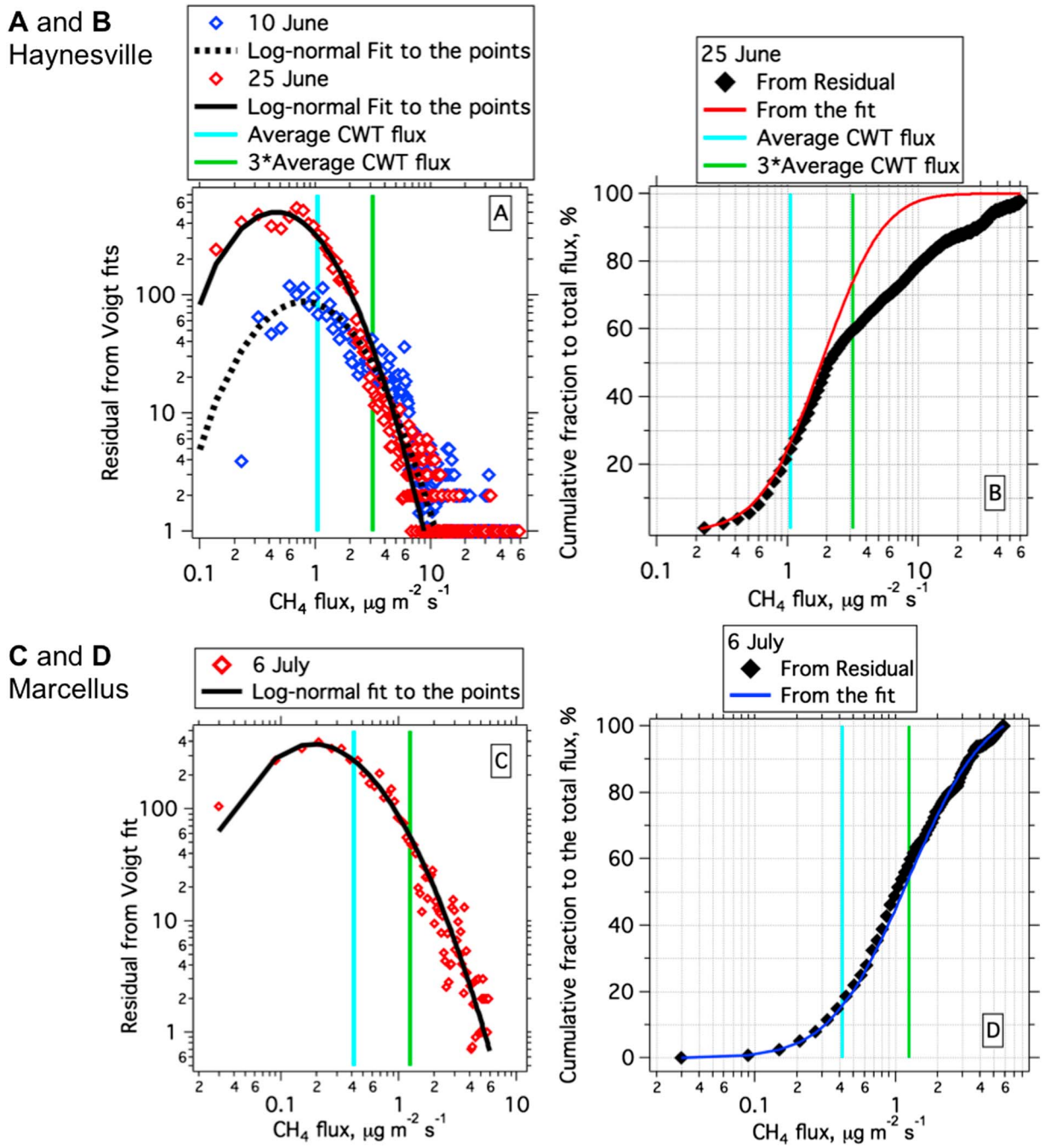

Figure 11. (a) Residuals from Voigt fits of CH_4 flux on 10 June (blue) and 25 June (red) over the Haynesville shale gas play region. The black solid and dashed lines are the lognormal fits to data points. The averaged CWT flux and 3 times of the averaged CWT flux on 25 June are also shown. (b) Cumulative distribution of CH_4 flux measured on 10 and 25 June. (c) Residuals from Voigt fit of CH_4 flux on 6 July over the Marcellus shale gas play. The averaged CWT flux and 3 times of the averaged CWT flux determined on this flight are also shown. (d) Cumulative distribution of CH_4 flux measured on 6 July.

flights over the Haynesville is not available. The C-130 only flew over the middle of the extraction region, and no effective characterization of upwind and downwind regions was made. The NOAA WP-3D flight on 10 June was not used for the mass balance method either, due to the absence of a constant wind field [*Peischl et al.*, 2015]. The inherent assumptions in the mass balance method allow this technique to be applied only when appropriate meteorological conditions are met [e.g., *Trainer et al.*, 1995]. The restriction also affected other mass balance studies in the literature. For example, only one out of 12 flights conducted in the Uintah Basin, Utah, was suitable for emission estimates based on the mass balance method [*Karion et al.*, 2013]. The

successful implementation of eddy covariance method to the WP-3D flight on 10 June suggests that eddy covariance method can be applied (at least) sometimes when favorable meteorological conditions to use the mass balance method are either not met or difficult to obtain. The estimates from the eddy covariance method also provide an independent test of the mass balance method. Therefore, our results indicate that the airborne eddy covariance method could be a powerful alternative technique to estimate emissions from oil and gas extraction activities.

3.4.3. The Distribution of Methane Emissions

Besides absolute emissions, the results of eddy covariance flux over oil and gas production regions can provide additional information about the distribution of emission fluxes within an area. Distributions of residuals from Voigt fits for both the Haynesville flights (10 and 25 June) and the Marcellus flight (6 July) are shown in Figure 11. It is clear that the distributions of residuals on 25 June and 6 July illustrate small variations as low as 0.15 $\mu g\,m^{-2}\,s^{-1}$ and 0.1 $\mu g\,m^{-2}\,s^{-1}$, while the lowest on 10 June are 0.6 $\mu g\,m^{-2}\,s^{-1}$, owing to the higher random errors from CWT calculations on 10 June (Table 2). As discussed above, the residuals from the Voigt fits are indicative of the actual emission fluxes of CH_4 from different sources in the shale gas region. Distributions of CH_4 emission fluxes for all three flights generally follow a lognormal distribution, as indicated by fitting performance in Figure 11. However, an inability to describe data points with high fluxes ($>10\,\mu g\,m^{-2}\,s^{-1}$) based on the lognormal function is noticeable for the two Haynesville flights. Reanalysis of reported CH_4 emissions from both well sites of the Barnett shale gas play [*Eastern Research Group and Sage Environmental Consulting*, 2011] and equipment components of gas processing plants [*National Gas Machinery Laboratory et al*., 2006] reveals similar lognormal distributions (Figure S7 in the supporting information). This lognormal distribution is also in agreement with recent mobile measurements of CH_4 emissions in several shale basins in western U.S. [*Brantley et al*., 2014]. The long-tailed structure of lognormal distribution implies that a small proportion of the facilities ("superemitters") make a disproportionate contribution to total CH_4 emissions.

High-emission regions (HERs) within a shale play are defined here as areas with a flux 3 times higher than the regional average. The averaged CWT fluxes determined in each basin are used as the surrogate of regional average. Figures 11b and 11d show cumulative fractions of the total CH_4 fluxes for flights on 25 June and 6 July, representing the Haynesville and Marcellus shale plays, respectively. The flight on 10 June is not used for this analysis, because the number of low-flux data points may be underestimated as a result of high random errors. The number of data points defined as HER accounts for 5% and 9% of the number of data points in Figures 11b and 11d, respectively. However, the contributions of these HERs to the determined CH_4 emission fluxes are determined to be 26% and 45% for the Haynesville flight (25 June) and the Marcellus flight (6 July), respectively. It is also notable that using the fitted lognormal curve to calculate the cumulative flux distribution underestimates the fraction contributed by HER for the flight on 25 June.

Another method to get more information on the distribution of CH_4 emissions within shale plays is peak analysis. The ten highest peaks (THPs) in the time series of CWT CH_4 fluxes are identified for all three WP-3D flights (Figure S8 in the supporting information). As discussed above, these high-flux peaks are associated with large facilities or large-density wells with high emission rates. The 10 highest peaks contribute 28%–39% and 18% of the determined CH_4 fluxes in the Haynesville and Marcellus shale plays, respectively (Table 2).

These two calculations (HER and THP) suggest that a small area or a small number of facilities contribute disproportionally to the total CH_4 emission fluxes in the areas represented by the flux footprints of the aircraft. Our results shown here are at least qualitatively similar with previous estimates in the literature [*Brandt et al*., 2014; *Subramanian et al*., 2015]. *Caulton et al*. [2014] showed that emissions from a small area with 1% of wells contribute 4–30% of total CH_4 emissions in southwestern Pennsylvania. It was also reported that 10% of well sites in the Barnett shale play accounted for 70% of CH_4 emissions [*Alvarez et al*., 2012]. Recent site-level measurements from compressor stations indicated the highest emitting 10% of sites contributed 50% of the total CH_4 emissions [*Subramanian et al*., 2015].

We note that the distributions of eddy covariance fluxes from aircraft measurement may be somewhat different from the emission distribution of individual wells, since each airborne flux estimate is the weighted average of emissions from a certain source contribution area (i.e., footprint). The inherent

averaging processes decrease the possibility to obtain extremely low or high values from the airborne flux measurements; i.e., all of the flux data points are prone to be closer to the regional average. Thus, our two calculations (HER and THP) may underestimate the contributions from superemitters in the shale gas regions. Since eddy covariance footprint in the WP-3D flights only cover 5–20% of the total production areas in the WP-3D flights, the undersampling and/or misdetection of some large emitters may also result in additional biases for emission distributions in the whole shale play.

4. Conclusions

Two aircrafts (NCAR C-130 and NOAA WP-3D) flew over two shale gas extraction regions in the summer of 2013. Enhancement ratios between CH_4 and different VOCs indicate that oil and gas emissions were the dominant sources for these species in the boundary layer over shale gas extraction regions.

High-time-resolution data for CH_4, selected VOC species, and vertical wind speed were recorded during two C-130 flights over the Haynesville shale play. The eddy covariance method was used to determine vertical fluxes of CH_4 and selected VOC species for the two research flights. We observed strong correlations of CH_4 and benzene fluxes from a hot spot during one C-130 flight. The enhancement ratio of CH_4 flux to benzene flux over a flux hot spot is consistent with that derived from concentrations. Spectral analysis suggests that 1 Hz data can be used for eddy covariance measurements on aircraft with sufficient accuracy for identifying and quantifying CH_4 sources including hot spots. The eddy covariance method was applied to calculate CH_4 fluxes from the NOAA WP-3D data sets over the Haynesville and Marcellus shale gas plays. Calculated CH_4 fluxes using the eddy covariance technique show agreement within the combined uncertainties with the results obtained from another independent technique (the mass balance method). Two WP-3D flights (10 and 25 June) with similar flight patterns over the Haynesville shale play also yielded comparable eddy covariance CH_4 fluxes. The successful implement of eddy covariance method to the WP-3D flight on 10 June suggests that eddy covariance method can be applied in some circumstances when favorable meteorological conditions to use the mass balance method are either not met or difficult to obtain. Our results demonstrate that the eddy covariance method provides a reliable alternative and complimentary technique for quantifying emissions from oil and gas extraction activities.

Statistical analysis of flux results indicates that random errors in CWT fluxes need to be considered for the determination of low-magnitude fluxes. Random errors of the CWT calculation could be described by a zero-centered Voigt distribution. By subtracting random errors, the distribution of emission fluxes could be derived. Emission strengths of CH_4 in a shale gas extraction region follow a lognormal distribution. Statistical analysis of CWT fluxes shows that emissions from a small number of facilities or a small areal extent (i.e., ~10%) are responsible for up to 40% of the total emissions in the Haynesville and Marcellus shale gas regions.

In this study, we use the eddy covariance technique to quantify the methane emissions from the Haynesville and Marcellus shale gas regions, and we demonstrate that the estimates from this study are consistent with those by the mass balance method in *Peischl et al.* [2015]. However, most of the flight patterns shown in this study were not optimized for to conduct airborne eddy covariance flux measurements. As shown in section 3.4.1, lower flight altitudes, repeated flight legs, measurements of flux divergence at several flight altitudes, and larger coverage of a shale gas basin would reduce uncertainties of measured eddy covariance fluxes to derive surface emission fluxes. These flight strategies will be implemented in future airborne campaigns (e.g., Shale Oil and Natural Gas Nexus, www.esrl.noaa.gov/csd/projects/songnex) with the aim to measure emission fluxes over other oil and gas production regions using eddy covariance techniques.

Acknowledgments
This work is partially funded by the NOAA's Health of the Atmosphere Program and Atmospheric Chemistry, Carbon Cycles, and Climate Program. The National Center for Atmospheric Research (NCAR) is sponsored by the U.S. National Science Foundation. A.B.G. was partially supported by the Laboratory Directed Research and Development program at PNNL. T.K. was supported by the EC Seventh Framework Program (Marie Curie Reintegration Program, "ALP-AIR", grant 334084). NCAR C-130 data during NOMADSS are provided by NCAR/EOL under sponsorship of the National Science Foundation (http://data.eol.ucar.edu). NOAA WP-3D data during SENEX are available at http://esrl.noaa.gov/csd/groups/csd7/measurements/2013senex.

References

Allen, D. T., et al. (2013), Measurements of methane emissions at natural gas production sites in the United States, *Proc. Natl. Acad. Sci. U.S.A.*, *110*(44), 17,768–17,773.

Alvarez, R. A., S. W. Pacala, J. J. Winebrake, W. L. Chameides, and S. P. Hamburg (2012), Greater focus needed on methane leakage from natural gas infrastructure, *Proc. Natl. Acad. Sci. U.S.A.*, *109*(17), 6435–6440.

Apel, E. C., et al. (2010), Chemical evolution of volatile organic compounds in the outflow of the Mexico City Metropolitan area, *Atmos. Chem. Phys.*, *10*(5), 2353–2375.

Aubinet, M., T. Vesala, and D. Papale (2012), *Eddy Covariance: A Practical Guide to Measurement and Data Analysis*, Springer, Heidelberg, Germany.

Borbon, A., et al. (2013), Emission ratios of anthropogenic volatile organic compounds in northern mid-latitude megacities: Observations versus emission inventories in Los Angeles and Paris, *J. Geophys. Res. Atmos.*, *118*, 2041–2057, doi:10.1002/jgrd.50059.
Born, M., H. Dorr, and I. Levin (1990), Methane consumption in aerated soils of the temperate zone, *Tellus, Ser. B*, *42*(1), 2–8.
Brandt, A. R., et al. (2014), Methane leaks from North American Natural Gas Systems, *Science*, *343*(6172), 733–735.
Brantley, H. L., E. D. Thoma, W. C. Squier, B. B. Guven, and D. Lyon (2014), Assessment of methane emissions from oil and gas production pads using mobile measurements, *Environ. Sci. Technol.*, *48*(24), 14,508–14,515.
Caulton, D. R., et al. (2014), Toward a better understanding and quantification of methane emissions from shale gas development, *Proc. Natl. Acad. Sci. U.S.A.*, *111*(17), 6237–6242.
Eastern Research Group, and Sage Environmental Consulting (2011), City of Fort Worth Natural Gas Air Quality Study. [Available at http://fortworthtexas.gov/gaswells/default.aspx?id=87074.Rep.]
Edwards, P. M., et al. (2014), High winter ozone pollution from carbonyl photolysis in an oil and gas basin, *Nature*, *514*, 351–354.
EIA (2013), U.S. expected to be largest producer of petroleum and natural gas hydrocarbons in 2013.
Field, R. A., J. Soltis, M. C. McCarthy, S. Murphy, and D. C. Montague (2015), Influence of oil and gas field operations on spatial and temporal distributions of atmospheric non-methane hydrocarbons and their effect on ozone formation in winter, *Atmos. Chem. Phys.*, *15*(6), 3527–3542.
Gilman, J. B., B. M. Lerner, W. C. Kuster, and J. A. de Gouw (2013), Source signature of volatile organic compounds from oil and natural gas operations in northeastern Colorado, *Environ. Sci. Technol.*, *47*(3), 1297–1305.
Gordon, M., S. M. Li, R. Staebler, A. Darlington, K. Hayden, J. O'Brien, and M. Wolde (2015), Determining air pollutant emission rates based on mass balance using airborne measurement data over the Alberta oil sands operations, *Atmos. Meas. Tech. Discuss.*, *8*(5), 4769–4816.
Helmig, D., C. R. Thompson, J. Evans, P. Boylan, J. Hueber, and J. H. Park (2014), Highly elevated atmospheric levels of volatile organic compounds in the Uintah Basin, Utah, *Environ. Sci. Technol.*, *48*(9), 4707–4715.
Hiller, R. V., B. Neininger, D. Brunner, C. Gerbig, D. Bretscher, T. Kunzle, N. Buchmann, and W. Eugster (2014), Aircraft-based CH_4 flux estimates for validation of emissions from an agriculturally dominated area in Switzerland, *J. Geophys. Res. Atmos.*, *119*, 4874–4887, doi:10.1002/2013JD020918.
Karion, A., et al. (2013), Methane emissions estimate from airborne measurements over a western United States natural gas field, *Geophys. Res. Lett.*, *40*, 4393–4397, doi:10.1002/grl.50811.
Karl, T., E. Apel, A. Hodzic, D. D. Riemer, D. R. Blake, and C. Wiedinmyer (2009), Emissions of volatile organic compounds inferred from airborne flux measurements over a megacity, *Atmos. Chem. Phys.*, *9*(1), 271–285.
Karl, T., P. K. Misztal, H. H. Jonsson, S. Shertz, A. H. Goldstein, and A. B. Guenther (2013), Airborne flux measurements of BVOCs above Californian Oak Forests: Experimental investigation of surface and entrainment fluxes, OH densities, and Damköhler numbers, *J. Atmos. Sci.*, *70*(10), 3277–3287.
Kemball-Cook, S., A. Bar-Ilan, J. Grant, L. Parker, J. Jung, W. Santamaria, J. Mathews, and G. Yarwood (2010), Ozone impacts of natural gas development in the Haynesville Shale, *Environ. Sci. Technol.*, *44*(24), 9357–9363.
Khelif, D., S. P. Burns, and C. A. Friehe (1999), Improved wind measurements on research aircraft, *J. Atmos. Oceanic Technol.*, *16*(7), 860–875.
Kim, K.-H., S. Baek, Y.-J. Choi, Y. Sunwoo, E.-C. Jeon, and J. H. Hong (2006), The emissions of major aromatic VOC as landfill gas from urban landfill sites in Korea, *Environ. Monit. Assess.*, *118*(1–3), 407–422.
Kirchstetter, T. W., B. C. Singer, R. A. Harley, G. R. Kendall, and W. Chan (1996), Impact of oxygenated gasoline use on California light-duty vehicle emissions, *Environ. Sci. Technol.*, *30*(2), 661–670.
Kljun, N., P. Kastner-Klein, E. Fedorovich, and M. W. Rotach (2004), Evaluation of Lagrangian footprint model using data from wind tunnel convective boundary layer, *Agric. For. Meteorol.*, *127*(3–4), 189–201.
Lenschow, D. H., J. Mann, and L. Kristensen (1994), How long is long enough when measuring fluxes and other turbulence statistics?, *J. Atmos. Oceanic Technol.*, *11*(3), 661–673.
Mauder, M., R. L. Desjardins, and I. MacPherson (2007), Scale analysis of airborne flux measurements over heterogeneous terrain in a boreal ecosystem, *J. Geophys. Res.*, *112*, D13112, doi:10.1029/2006JD008133.
McKenzie, L. M., R. Guo, R. Z. Witter, D. A. Savitz, L. S. Newman, and J. L. Adgate (2014), Birth outcomes and maternal residential proximity to natural gas development in rural Colorado, *Environ. Health Perspect.*, *122*(4), 412–417.
Metzger, S., et al. (2013), Spatially explicit regionalization of airborne flux measurements using environmental response functions, *Biogeosciences*, *10*(4), 2193–2217.
Miller, S. M., et al. (2013), Anthropogenic emissions of methane in the United States, *Proc. Natl. Acad. Sci. U.S.A.*, *110*(50), 20,018–20,022.
Misztal, P. K., T. Karl, R. Weber, H. H. Jonsson, A. B. Guenther, and A. H. Goldstein (2014), Airborne flux measurements of biogenic isoprene over California, *Atmos. Chem. Phys.*, *14*(19), 10,631–10,647.
Montzka, S. A., E. J. Dlugokencky, and J. H. Butler (2011), Non-CO_2 greenhouse gases and climate change, *Nature*, *476*(7358), 43–50.
National Gas Machinery Laboratory, C. E., and Innovative Environmental Solutions (2006), Cost-effective directed inspection and maintenance control opportunities at five gas processing plants and upstream gathering compressor stations and well sites, Rep., EPA.
Park, J. H., A. H. Goldstein, J. Timkovsky, S. Fares, R. Weber, J. Karlik, and R. Holzinger (2013), Eddy covariance emission and deposition flux measurements using proton transfer reaction–time of flight–mass spectrometry (PTR-TOF-MS): Comparison with PTR-MS measured vertical gradients and fluxes, *Atmos. Chem. Phys.*, *13*(3), 1439–1456.
Peischl, J., et al. (2012), Airborne observations of methane emissions from rice cultivation in the Sacramento Valley of California, *J. Geophys. Res.*, *117*, D00V25, doi:10.1029/2012JD017994.
Peischl, J., et al. (2015), Quantifying atmospheric methane emissions from the Haynesville, Fayetteville, and northeastern Marcellus shale gas production regions, *J. Geophys. Res. Atmos.*, *120*, 2119–2139, doi:10.1002/2014JD022697.
Pétron, G., et al. (2014), A new look at methane and nonmethane hydrocarbon emissions from oil and natural gas operations in the Colorado Denver-Julesburg Basin, *J. Geophys. Res. Atmos.*, *119*, 6836–6852, doi:10.1002/2013JD021272.
Reba, M. L., T. E. Link, D. Marks, and J. Pomeroy (2009), An assessment of corrections for eddy covariance measured turbulent fluxes over snow in mountain environments, *Water Resour. Res.*, *45*, W00D38, doi:10.1029/2008WR007045.
Rhee, T. S., A. J. Kettle, and M. O. Andreae (2009), Methane and nitrous oxide emissions from the ocean: A reassessment using basin-wide observations in the Atlantic, *J. Geophys. Res.*, *114*, D12304, doi:10.1029/2008JD011662.
Rosenberg, P. D., et al. (2014), Quantifying particle size and turbulent scale dependence of dust flux in the Sahara using aircraft measurements, *J. Geophys. Res. Atmos.*, *119*, 7577–7598, doi:10.1002/2013JD021255.
Schnell, R. C., S. J. Oltmans, R. R. Neely, M. S. Endres, J. V. Molenar, and A. B. White (2009), Rapid photochemical production of ozone at high concentrations in a rural site during winter, *Nat. Geosci.*, *2*(2), 120–122.
Subramanian, R., et al. (2015), Methane emissions from natural gas compressor stations in the transmission and storage sector: Measurements and comparisons with the EPA greenhouse gas reporting program protocol, *Environ. Sci. Technol.*, *49*(5), 3252–3261.

Torrence, C., and G. P. Compo (1998), A practical guide to wavelet analysis, *Bull. Am. Meteorol. Soc.*, *79*(1), 61–78.
Trainer, M., B. A. Ridley, M. P. Buhr, G. Kok, J. Walega, G. Hübler, D. D. Parrish, and F. C. Fehsenfeld (1995), Regional ozone and urban plumes in the southeastern United States: Birmingham, A case study, *J. Geophys. Res.*, *100*(D9), 18,823–18,834, doi:10.1029/95JD01641.
US Environmental Protection Agency (2014), Inventory of U.S. greenhouse gas emissions and sinks: 1990–2012*, Rep. EPA 430-R-414-003*, U.S. Environmental Protection Agency, Washington, D. C.
Warneke, C., et al. (2007), Determination of urban volatile organic compound emission ratios and comparison with an emissions database, *J. Geophys. Res.*, *112*, D10S47, doi:10.1029/2006JD007930.
Warneke, C., et al. (2013), Photochemical aging of volatile organic compounds in the Los Angeles basin: Weekday-weekend effect, *J. Geophys. Res. Atmos.*, *118*, 5018–5028, doi:10.1002/jgrd.50423.
Warneke, C., et al. (2014), Volatile organic compound emissions from the oil and natural gas industry in the Uinta Basin, Utah: Point sources compared to ambient air composition, *Atmos. Chem. Phys.*, *14*(8), 10,977–10,988.
Warneke, C., et al. (2015), PTR-QMS vs. PTR-TOF comparison in a region with oil and natural gas extraction industry in the Uintah Basin in 2013, *Atmos. Meas. Tech.*, *8*, 411–420.
Weil, J., and T. Horst (1992), Footprint estimates for atmospheric flux measurements in the convective boundary layer, *Precip. Scavenging Atmos. Surf. Exch.*, *2*, 717–728.
White, W., J. Anderson, D. Blumenthal, R. Husar, N. Gillani, J. Husar, and W. Wilson (1976), Formation and transport of secondary air pollutants: Ozone and aerosols in the St. Louis urban plume, *Science*, *194*(4261), 187–189.
Yuan, B., C. Warneke, M. Shao, and J. A. de Gouw (2014), Interpretation of volatile organic compound measurements by proton-transfer-reaction mass spectrometry over the deepwater horizon oil spill, *Int. J. Mass Spectrom.*, *358*, 43–48.
Zulueta, R. C., W. C. Oechel, J. G. Verfaillie, S. J. Hastings, B. Gioli, W. T. Lawrence, and K. T. Paw U (2013), Aircraft regional-scale flux measurements over complex landscapes of mangroves, desert, and marine ecosystems of Magdalena Bay, Mexico, *J. Atmos. Oceanic Technol.*, *30*(7), 1266–1294.